Advanced Energy Materials

ADVANCED ENERGY MATERIALS
www.advenergymat.de

RESEARCH ARTICLE OPEN ACCESS

Electrolyte Confinement Enables a Continuous Transition From Battery-Like to Capacitor-Like Na^+ Storage via Solvent Co-Intercalation

Yoga Trianzar Malik[1,2] | Samra[1,2] | Mennatalla Elmanzalawy[1,2] | Thomas Pechon[1,2,3] | Jameela Karol[1,2] | Jaehoon Choi[1,2] | Robert Leiter[1,2] | Maciej Tobis[1,2] | Wan-Yu Tsai[4,5] | Xiaolin Liu[6] | De-en Jiang[6] | Simon Fleischmann[1,2]

[1]Helmholtz Institute Ulm (HIU), Helmholtzstr. 11, Ulm, Germany | [2]Karlsruhe Institute of Technology (KIT), Karlsruhe, Germany | [3]Département de Chimie, Ecole Normale Supérieure – PSL, Paris, France | [4]UMR 8520 – IEMN, CNRS, Université de Lille, Université Polytechnique Hauts-de-France, Lille, France | [5]CNRS FR 3459, Réseau sur le Stockage Electrochimique de l'Energie (RS2E), Amiens, France | [6]Department of Chemical and Biomolecular Engineering, Vanderbilt University, Nashville, Tennessee, USA

Correspondence: Maciej Tobis (maciej.tobis@kit.edu) | Simon Fleischmann (simon.fleischmann@kit.edu)

Received: 10 February 2026 | **Revised:** 5 May 2026 | **Accepted:** 12 June 2026

Keywords: ion intercalation | pseudocapacitance | sodium-ion battery

ABSTRACT

Understanding how electrolyte solvation and nanoconfinement govern sodium-ion intercalation is essential for designing high-power sodium storage electrodes. Here, we use a model series of hydrogen titanates with systematically expanded interlayer spacings to investigate how the degree of electrolyte confinement governs the transition from battery-like toward capacitor-like Na^+ storage signatures. In carbonate-based electrolyte, all materials form resistive interphases, exhibit pronounced charge transfer resistance, and show conventional sluggish kinetics. In contrast, diglyme-based electrolyte enables solvent co-intercalation of Na^+-diglyme complexes, limits interphase formation, and produces rectangular/capacitor-like CV signatures with strongly reduced interfacial impedance and excellent high-rate performance. Ex situ TEM analysis and operando dilatometry confirm reduced interphase growth and reversible co-intercalation-induced lattice expansion in diglyme. These findings provide direct evidence for a confinement-controlled continuum between Faradaic and capacitive Na^+ storage and highlight electrolyte solvation and electrode nanoconfinement co-design as a powerful strategy toward high-power sodium storage.

1 | Introduction

Sodium-ion batteries (SIBs) are attractive alternatives to complement lithium-ion batteries due to the abundance and lower cost of sodium [1]. However, achieving high power performance remains challenging, particularly on the anode side. Hard carbons are today's dominant SIB anodes and operate at very low potentials near 0 V versus Na^+/Na, which poses a risk of sodium plating on the electrode surface during fast charging [2]. In conventional carbonate-based electrolytes, a substantial solid-electrolyte interphase (SEI) forms, adding interfacial impedance and slowing ion insertion, thereby limiting rate capability. Such limitations become even more critical in sodium-ion capacitors (SICs), where the negative electrode must sustain high currents to match the capacitive positive electrode [3].

Yoga Trianzar Malik and Samra contributed equally to this work.

To overcome these limitations, alternative anode materials that operate at slightly higher potentials and exhibit fast charge storage capability are needed. Layered titanates are promising candidates because they intercalate Na^+ between around 0.3 and 0.7 V vs. Na^+/Na, reducing the risk of plating, and their structure offers exceptional tunability of the interlayer environment [4–7]. Hydrogen titanates (HTOs), in particular, contain nanoconfined protons and/or water that can be replaced through ion exchange or molecular pillaring [8–10]. Their interlayer chemistry strongly influences charge storage, as demonstrated by reports of H_2 evolution from reducing interlayer protons [11], or Li^+/solvent co-intercalation [12], or increased Na^+ storage in alkylamine-pillared phases [13].

In parallel, a complementary concept has emerged from solvent co-intercalation research [14, 15]. Adelhelm and coworkers showed that Na^+-diglyme complexes can intercalate into graphite [16, 17] and proposed that these glyme-based systems may operate with strongly suppressed SEI formation [18], even at strongly reducing electrode potentials near 0 V versus Na^+/Na, a hypothesis that continues to be actively debated but has the potential to strongly reduce interfacial impedance. Moreover, solvent co-intercalation is, in principle, an attractive mechanism to enable high-rate capability because the absence of full desolvation at the electrochemical interface has the potential to strongly reduce charge transfer resistance [14]. Recent work by Wei and coworkers demonstrated that co-intercalation of such Na^+-diglyme complexes can yield capacitor-like electrochemical characteristics, which hold promise for use in sodium-ion capacitors [19, 20]. These aspects highlight the decisive role of solvation and electrolyte stability, in addition to the intrinsic host structure, in dictating Na^+ storage behavior.

We recently proposed a broader hypothesis that electrochemical charge storage in confined electrolytes forms a continuum between electric double-layer (capacitive) and Faradaic intercalation mechanisms, governed by the degree of ion solvation and resulting ion-host interaction [21]. Under this assumption, nanoconfinement and incomplete desolvation can yield capacitor-like electrochemical signatures even in materials traditionally considered Faradaic intercalation hosts. Layered titanates with tunable interlayer spacing therefore provide an ideal experimental platform to probe this continuum directly.

Here, we synthesize a series of hydrogen tetratitanate-based materials ($H_2Ti_4O_9$) with systematically increased interlayer spacing and investigate their Na^+ storage properties in carbonate- and diglyme-based electrolytes. We show that in carbonate electrolytes, all materials undergo SEI formation and exhibit conventional, diffusion-limited intercalation with significant interfacial impedance. In contrast, in diglyme, expanding the interlayer galleries enables highly reversible Na^+ storage with progressively more capacitor-like, high-rate behavior, while exhibiting strongly reduced charge transfer resistance and minimal interfacial impedance. These results provide direct experimental support for a confinement-controlled continuum in this model system and demonstrate a powerful strategy for designing high-rate sodium anodes using confined electrolytes.

2 | Experimental Section

2.1 | Materials Synthesis

Hydrogen tetratitanate ($H_2Ti_4O_9$, referred to as HTO) was synthesized through a two-step solid-state and wet-chemical method. The first step is the solid-state synthesis of potassium tetratitanate ($K_2Ti_4O_9$). It was synthesized by heating a mixture of potassium carbonate (K_2CO_3, VWR Chemicals) and titanium dioxide (TiO_2, Thermo Scientific) in a 1:3.5 molar ratio at 800°C for 20 h in a muffle furnace (Nabertherm P330), followed by an additional 20 h after grinding with a mortar and pestle. The second step to obtain HTO is to stirr 1 g of $K_2Ti_4O_9$ in 200 mL of 2 M hydrochloric acid (HCl, VWR Chemicals) in a round-bottom flask for 3 days at 60°C under reflux. The resulting product was then vacuum-filtered, washed with deionized (DI) water, and dried at room temperature under airflow before further characterization.

Alkylammonium-pillared HTOs, namely HTO-propylammonium (HTO-PA) and HTO-octylammonium (HTO-OA), were synthesized by stirring 200 mg of the baseline HTO powder in 6.66 mL of 50 vol.% aqueous solutions of propylamine (C_3H_9N, Thermo Scientific) or octylamine ($C_8H_{19}N$, Thermo Scientific), respectively, for 72 h at room temperature. The alkylammonium-pillared HTO powders were recovered by vacuum filtration, then washed several times with DI water until neutral pH was reached, and left to dry in circulating air at room temperature.

2.2 | Structural Characterization

Powder X-ray diffraction (XRD) patterns of the samples were obtained using a Bruker D8 Advance equipped with a Cu Kα radiation source ($\lambda = 0.15406$ nm) and a LYNXEYE XE-T detector. The patterns were recorded in Bragg–Brentano mode in the 2θ range between 2° and 60° with a 0.02° step size.

Scanning electron microscopy (SEM) imaging was performed using a ZEISS Crossbeam 340 electron microscope operated at 5 kV and a working distance of 7.4 mm.

Thermogravimetric analysis was carried out using a NETZSCH TG 209 F1 Libra thermal analyzer under a mixed N_2/O_2 atmosphere. The temperature was increased to up to 600°C at a ramp rate of 5°C/min.

2.3 | Electrode Preparation

The synthesized HTO powders were used to make electrode slurries where the active material, conductive carbon (C-NERGY Super C65), and polyvinylidene fluoride (PVDF, Solvay) binder (2 wt.% PVDF dissolved in *N*-Methyl-2-pyrrolidone, NMP, Thermo Scientific) with a mass ratio of 8:1:1 was ground using a pestle and mortar, then homogenized using a speed mixer (Thinky) at 2000 rpm for 10 min. The slurry was then cast onto carbon-coated Al current collectors (20 µm thickness, Welcos) using a doctor blade with a wet film thickness set to 60 µm, resulting in mass loadings of ca. 0.6–0.7 mg/cm^2. The low mass loading is favorable to avoid kinetic limitations caused by

electrode architecture, allowing the study to focus on fundamental materials properties. The cast slurries were set to dry overnight in circulating air, then subsequently cut into 12-mm discs and dried overnight in vacuum at room temperature. Elevated drying temperatures were avoided due to the volatility of confined interlayer species, particularly propylammonium. Prior to use, the electrode films were compacted using a hydraulic press set to 5 tons for 30 s.

2.4 | Electrochemical Measurements

Standard electrochemical measurements (CV and GCD) were performed in coin cells (type CR2032) in a two-electrode configuration against 12 mm diameter Na disc electrodes (Acros Organics, 99.8%), and a 19 mm diameter Whatman glass microfiber (grade GF/A) was used as a separator. The cells were filled with 150 µL of electrolyte, namely either 1 M $NaPF_6$ (battery grade, FluoroChem) in a 1:1 vol.% mixture of ethylene carbonate/propylene carbonate (EC/PC, battery grade, UBE) or 1 M $NaPF_6$ in bis(2-methoxyethyl)ether (diglyme/2G, 99.5%, Thermo Scientific).

The electrochemical experiments were conducted with potentiostats from Biologic (VMP-3e, VMP-300) with the cells placed in temperature-controlled climatic chambers set at 20°C.

Electrochemical impedance spectroscopy (EIS) measurements were performed using a three-electrode custom-built polyether ether ketone (PEEK) cell. These contained HTO-based materials as the working electrode and sodium metal for both the counter electrode (12 mm disc) and the separate quasi-reference electrode (a small piece placed in the side channel of the cell, contacted by a titanium screw). Further details on the custom-built PEEK cell were previously published [22]. EIS used a frequency range of 200 kHz to 10 mHz with a 10 mV amplitude and two data averages per frequency. Ten points per decade were collected. Impedance spectra were fitted in the RelaxIS software by considering a proportional weighting method for all range of frequency.

Electrochemical dilatometry (ECD) measurements were conducted using an ECD-4-nano dilatometer (EL-Cell). The HTO-based working electrodes were prepared by using slurries containing 60 wt.% active material, 30 wt.% carbon black and 10 wt.% PVDF binder dissolved in a 2 wt.% NMP solution. The slurries were then directly drop-cast onto the piston of the dilatometry cell and dried at 60°C under vacuum for 12 h. Then, the coatings were compressed using a hydraulic press set to 1 ton for 10 s. The resulting mass loading of the electrode is 4–5 mg/cm^2.

The dilatometer was then assembled in an Ar-filled glovebox. It was assembled in a half-cell setup using an 8 mm Na metal disc acting as the counter electrode. Approximately 300–350 µL of electrolyte was injected onto the T-Frit, and the working electrode, coated directly onto the piston, was placed on top of the T-Frit. The cell was sealed using the screw cap unit with a membrane to ensure airtightness and electrical contact. Following transfer from the glovebox, the sensor head was attached, and the cell was connected to a docking station (PAT-Stand-1, EL-Cell) housed in a temperature-controlled chamber (22°C) linked to a potentiostat (Bio-Logic VMP3).

2.5 | Ex Situ Transmission Electron Microscopy Study

For the ex situ transmission electron microscopy (TEM) study, the HTO-based powder materials were dispersed in 10 mL NMP and sonicated for 5 min. The suspension was drop-cast onto a gold-coated TEM grid and dried under vacuum at 60°C for 24 h. The grid then acted as a current collector and was directly placed into a three-electrode Swagelok-type cell, and linear sweep voltammetry was performed at 0.5 mV/s from open-circuit potential (≈2.6 V vs. Na^+/Na) to 0.2 V versus Na^+/Na, followed by a 2 h hold. The cells were then disassembled in an Ar-filled glovebox (<0.5 ppm O_2 and H_2O), the grids were removed and rinsed with the respective solvent and sealed inside a Mel-Build Double Tilt LN2 Atmos Defend Holder and transferred to the microscope under inert conditions. (S)TEM imaging was performed using a ThermoFisher Talos F200i instrument. In addition to bright-field- (BF-TEM) and high-resolution TEM (HRTEM), we performed high-angle annular dark-field scanning transmission electron microscopy (HAADF–STEM) in conjunction with energy-dispersive X-ray spectroscopy (EDX) using Bruker DualX windowless EDX detectors to generate elemental maps.

2.6 | Computational Details

The initial structure of HTO-OA was constructed by extending our previously reported HTO model. Density functional theory (DFT) calculations were carried out using the Vienna ab initio Simulation Package (VASP) [23–25] with periodic boundary conditions. The interaction between core and valence electrons was described using the projector augmented wave (PAW) method [26]. Electron exchange–correlation effects were treated within the generalized gradient approximation (GGA) using the Perdew–Burke–Ernzerhof (PBE) [27] functional. Brillouin zone sampling was performed using a Monkhorst–Pack scheme with a maximum k-point spacing of <0.03 $Å^{-1}$, corresponding to a 1 × 6 × 1 k-point mesh [28]. A plane-wave energy cutoff of 520 eV was employed, and long-range van der Waals interactions were accounted for using Grimme's D3 dispersion correction [29]. Both the lattice parameters (cell shape and volume) and atomic positions were fully relaxed. Electronic self-consistency was achieved with an energy convergence criterion of 1×10^{-5} eV, and structure was optimized until the residual forces on each atom were less than 0.02 eV $Å^{-1}$. The d_{200} of the optimized structure was obtained using the VESTA [30] software.

3 | Results and Discussion

3.1 | Structural Characterization of the HTO Model Series

Hydrogen tetratitanate ($H_2Ti_4O_9$, HTO) is subjected to organic functionalization with n-alkylammonium pillars of different lengths, namely propylammonium (PA) and octylammonium (OA). During this functionalization procedure in aqueous solution, ammonium(NH_3^+)-terminated pillars become confined within the HTO interlayer space, where they exchange with the structural protons of HTO [12, 31]. This pillaring strategy enables

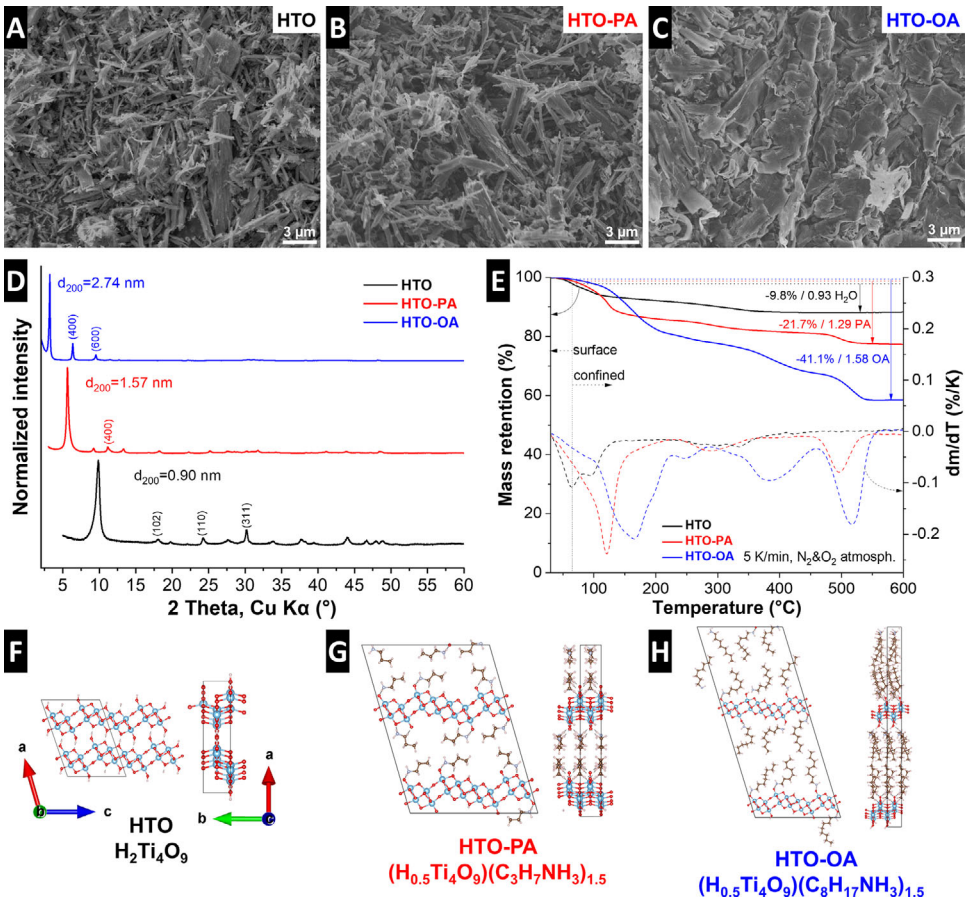

FIGURE 1 | Scanning electron micrographs of (A) HTO, (B) HTO-PA, and (C) HTO-OA powder samples. (D) XRD pattern and (E) TGA, including differential mass evolution plot of all samples. Optimized crystal structures for (F) HTO, (G) HTO-PA, and (H) HTO-OA from DFT calculations.

systematic tuning of the HTO interlayer spacing, consistent with our previous work [12].

Scanning electron micrographs of pristine HTO, HTO-PA, and HTO-OA (Figure 1A–C) reveal the morphological consequences of interlayer expansion. Pristine HTO consists of rod-like particles with a length of several micrometers. Pillaring with the smaller PA molecules maintains the rod-like morphology, although a modest increase in rod thickness is observed. In contrast, pillaring with large OA molecules leads to a notable swelling of the particles and slight rod deformations. The longer organic chains of OA induce a more crumpled, sheet-like morphology, consistent with stronger interlayer expansion and weaker interlayer cohesion. Importantly, no evidence of particle pulverization or dissolution–recrystallization is observed, indicating that pillaring proceeds topotactically and preserves the parent titanate framework. This supports the previously described [12] topotactic nature of the pillar confinement process in the HTO host.

X-ray diffraction (XRD, Figure 1D) confirms the successful synthesis of phase-pure, hydrated hydrogen tetratitanate ($H_2Ti_4O_9{\cdot}H_2O$) according to PDF 00–036-0655 via the solid-state and wet-chemical synthesis process. In its pristine state, HTO exhibits an interlayer spacing of ca. 0.90 nm shown by the dominant (200) reflection at 9.86° 2θ. The functionalization approach using PA or OA pillar molecules leads to a systematic expansion of the interlayer spacing to 1.57 and 2.74 nm, respectively, indicated by the significant shift of the (200) signal toward lower diffraction angles. The emergence of higher-order (400) and (600) reflections further indicates that interlayer expansion is homogeneous and preserves long-range structural order.

Thermogravimetric analysis (TGA) is conducted to estimate the chemical composition and pillar loading of the materials (Figure 1E). Heating of HTO-based samples to 600°C in an oxygen-containing atmosphere leads to the complete transformation of $H_2Ti_4O_9$ to 4 TiO_2 via dehydration [32], corresponding to a mass loss of 5.3 wt.%. Any additional mass loss can therefore be assigned to surface-adsorbed or interlayer-confined species. To differentiate between these contributions, we use the differential mass signal and observe two distinct mass loss steps in pristine hydrated HTO. The first process is assigned to the loss of surface water, whereas the subsequent step is attributed to confined crystal water. Quantification yields ca. 1 confined water molecule per tetratitanate unit, leading to an estimated structural formula of $H_2Ti_4O_9{\cdot}H_2O$, in agreement with XRD and previous reports [12]. For HTO-PA and HTO-OA, the thermogravimetric response can be interpreted in two broad temperature regimes. At lower temperatures (<200°C), contributions from weakly adsorbed species are expected, including surface water and possibly weakly bound amine-containing species. In contrast, the larger mass loss between ca. 350 C and 550°C is assigned to decomposition and/or combustion of the interlayer-confined organic pillars.

The significance of this higher-temperature process is that it supports the presence of more strongly incorporated organic species within the expanded interlayer structure, rather than only surface-adsorbed molecules. Based on the total pillar-related mass loss, the results reveal loadings between ca. 1.3 (PA) and 1.6 (OA) pillar molecules per tetratitanate. The amount of residual interlayer water is expected to be reduced in the pillared materials because the alkyl chains render the interlayer environment less favorable for water retention [33]. At the same time, residual interlayer water cannot be quantified independently with high confidence from TGA alone because low-temperature water loss may overlap with the release of weakly bound amine-containing species. The similar pillar loadings indicate that the number of interlayer-confined organic pillars per tetratitanate unit remains approximately constant across the pillared HTO series, while the interlayer spacing changes substantially with pillar length.

The experimentally derived crystallographic data and composition information are used to construct DFT-optimized structures of the host materials. Confirming our previous models for HTO and HTO-PA (Figure 1F,G),12 we additionally present the optimized structure for highly expanded HTO-OA (Figure 1H). In this configuration, OA molecules adopt a tilted bilayer arrangement within the HTO interlayer galleries, resulting in an interlayer spacing of 2.70 nm. Comparison of the experimental and DFT-simulated diffraction patterns for HTO-PA and HTO-OA shows good agreement in the positions of the low-angle reflections, supporting the proposed structural models and the interlayer spacings derived from them (Figure S1). The structural models illustrate how increasing pillar length enlarges the accessible interlayer gallery volume, which becomes relevant for Na^+ solvation and transport.

Taken together, the experimental and computational characterization demonstrates precise control over interlayer spacing in the HTO host lattice. Thus, this materials series provides a model system in which the degree of nanoconfinement within the interlayer galleries can be systematically tuned independently of the titanate framework. This structural tunability enables a direct investigation of how interlayer confinement governs Na^+ storage mechanisms.

3.2 | Electrochemical Na^+ Storage in Ether-Based Electrolyte

To evaluate the influence of HTO interlayer confinement on the resulting electrochemical Na^+ storage properties, cyclic voltammetry (CV, Figure 2A) was performed on the titanate series with systematically increasing interlayer spacing in an ether-based electrolyte (1 M $NaPF_6$ in diglyme). The CV of pristine HTO shows two broad redox features around 0.4 and 1.0 V versus Na^+/Na, indicative of a Faradaic intercalation process. Strikingly, the electrochemical response evolves systematically toward a rectangular, capacitor-like CV shape as the HTO interlayer spacing increases. The material with the largest interlayer spacing (HTO-OA) shows an almost ideal rectangular response between ca. 0.2 and 1.2 V. This evolution is consistent with the previously hypothesized confinement-driven transition from Faradaic to capacitive charge storage [21].

The specific sodiation capacity and rate handling behavior are further quantified using galvanostatic charge/discharge (GCD) experiments (Figure 2B). At a low rate of 50 mA/g, the maximum anodic/desodiation capacities are 97, 124, and 103 mAh/g for HTO, HTO-PA, and HTO-OA, respectively, when normalized to the total mass of the active material, i.e., the combined mass of the titanate host and the organic pillars. Because the heavier OA pillars contribute more inactive mass than PA, this gravimetric capacity trend does not directly reflect the degree of Na^+ uptake by the titanate host itself. After correcting for pillar mass and expressing the storage per tetratitanate unit ($H_2Ti_4O_9$), the maximum reversible (de)sodiation capacities correspond to 1.29 Na^+ for HTO, 1.92 Na^+ for HTO-PA, and 2.08 Na^+ for HTO-OA. This shows that the degree of Na^+ uptake by the host lattice increases with interlayer expansion, consistent with analogous Li^+ storage reported previously [12]. Overall, these maximum capacities lie within the typical range reported for titanate-based Na-storage electrodes (~90–120 mAh/g) [4, 34], while the main advance of the present work lies not in maximizing gravimetric capacity, but in revealing the systematic transition in charge storage mechanism upon interlayer expansion.

At elevated rates, the electrochemical differences between the materials become more pronounced. At 5 A/g, pristine HTO loses nearly all capacity, whereas HTO-PA and HTO-OA retain 46% and 59% of their initial capacities, respectively. The voltage profile of HTO-OA under these conditions remains sloping and linear, with lower polarization than HTO-PA (Figure S2). These high-rate results highlight the capacitor-like Na^+ storage characteristics of the most expanded HTO-OA in diglyme. While interlayer-confined organic pillars can, in principle, hinder ion transport by partially blocking diffusion pathways and storage sites [35, 36], the similar pillar loadings of HTO-PA and HTO-OA indicate that this effect should be comparable across the pillared samples, such that the systematic kinetic evolution is attributed primarily to the increasing interlayer spacing. It should be noted that these measurements were carried out at deliberately low mass loading (0.6–0.7 mg/cm^2) in order to minimize transport limitations arising from electrode architecture and to isolate the intrinsic materials effects.

The cycling stability of the HTO-based electrode materials was evaluated in half-cells over 1000 cycles (Figure S3). All electrodes show the most pronounced capacity loss within the first ~100 cycles, after which the capacity evolution stabilizes. Pristine HTO exhibits the fastest initial degradation, losing approximately 30% of its capacity during the first 100 cycles, whereas HTO-PA and HTO-OA show more moderate losses of ca. 12% and 20%, respectively. Upon extended cycling, pristine HTO continues to fade significantly, retaining only about 45% of its initial capacity after 1000 cycles. In contrast, HTO-PA retains ca. 67% and HTO-OA ca. 73% of their initial capacities. Overall, these results indicate that interlayer expansion leads to improved cycling stability compared to pristine HTO under the investigated conditions.

These observations open important mechanistic questions, as such high-rate capability is uncommon for typical SIB anodes operating close to an electrode potential of 0 V versus Na^+/Na. In particular, (1) to what extent interphases form at highly reductive electrode potentials, (2) whether solvent co-intercalation

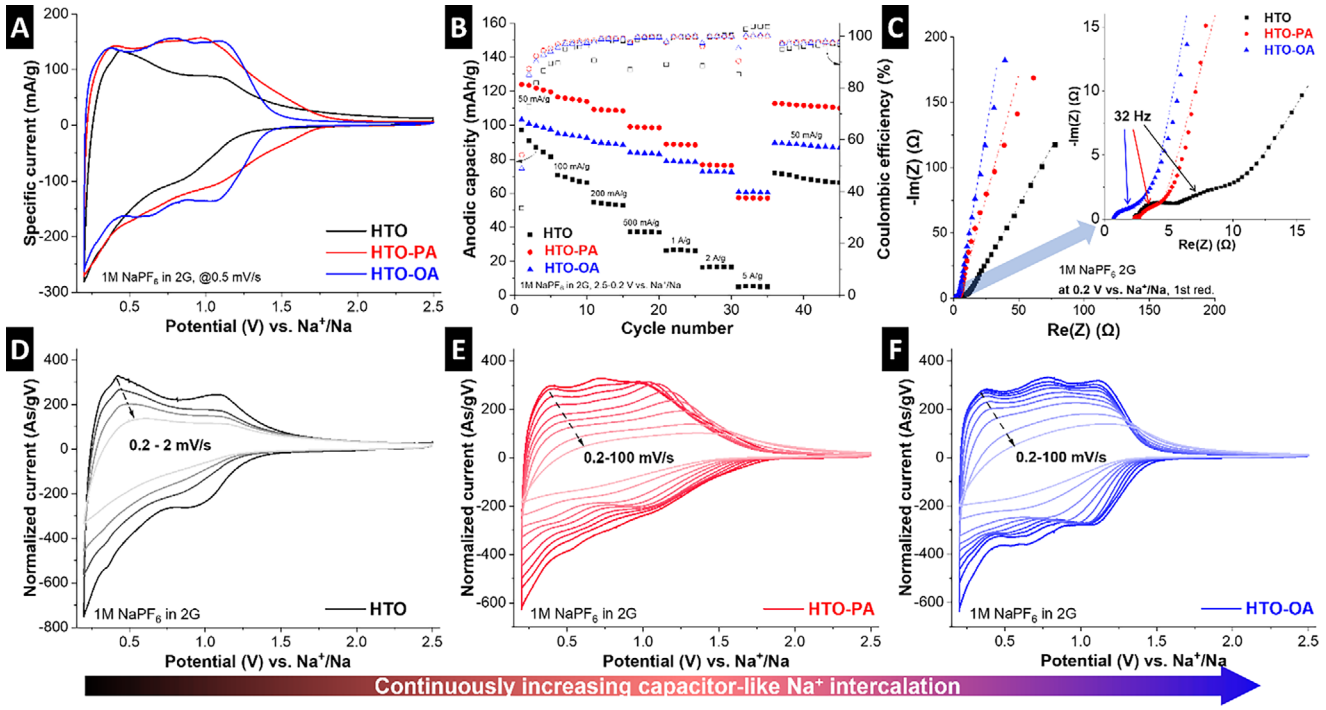

FIGURE 2 | Electrochemical characterization of HTO series in 1 M $NaPF_6$ in diglyme electrolyte. (A) Cyclic voltammograms at 0.5 mV/s, (B) Galvanostatic charge–discharge at rates from 50 mA/g to 5 A/g. (C) Nyquist plots recorded at stabilized electrode potentials of 0.2 V versus Na^+/Na, inset: zoomed-in view of mid-/high-frequency region. (D) *b*-value analysis of HTO using sweep rates between 0.2 and 2 mV/s, and (E), (F) of HTO-PA and HTO-OA using sweep rates between 0.2 and 100 mV/s.

contributes to reduced charge transfer resistance, and (3) what limits Na^+ transport in confined HTO environments?

To address these scientific questions, the charge storage kinetics were probed via electrochemical impedance spectroscopy (EIS). After the first electrode reduction to 0.2 V and reaching steady-state conditions, impedance spectra were recorded for all three electrodes of the series (Figure 2C). In the low-frequency region, the Nyquist plot of pristine HTO shows a sloping region with a phase angle $|\varphi| > 45°$ [37]. With increasing HTO interlayer spacing, the low-frequency response shifts progressively toward a capacitor-like regime, with HTO-OA exhibiting a nearly vertical line characteristic of capacitive behavior [38].

To better resolve the mid- to high-frequency regions, a zoom-in is shown in Figure 2C, inset. Pristine HTO exhibits two distinct semicircles, where the higher-frequency feature is commonly associated with the presence of an interfacial surface layer (e.g., SEI-related processes), while the lower-frequency feature is attributed to the Faradaic charge transfer step, which in conventional electrolytes includes ion desolvation [39]. Accordingly, equivalent-circuit analysis allows extraction of an interfacial resistance (R_{SEI}) and charge transfer resistance (R_{ct}) [40]. The impedance analysis is discussed in more detail in the supporting information, Figures S4 and S5.

With increasing interlayer spacing, the higher-frequency semicircle progressively diminishes and becomes negligible for HTO-OA, while R_{ct} is simultaneously reduced by approximately a factor of two compared to pristine HTO. These trends indicate that sodiation of expanded HTOs from diglyme electrolyte proceeds with strongly suppressed interphase resistance and markedly reduced charge transfer impedance, consistent with a transition toward desolvation-free Na^+ intercalation and capacitor-like kinetics in expanded host lattices. The fitted values of R_{SEI} and R_{ct} are summarized in Table 1 and are contrasted with the substantially larger resistances observed in the carbonate-based electrolyte discussed in a later section.

To further assess diffusion-limitations, *b*-value analysis [41, 42] was performed using the sweep rate (v) dependence of the measured current i in CVs according to the formula:

Where a and b are variables. In the limiting cases, the *b*-value of 0.5 defines an ideally semi-infinite diffusion-controlled current according to the Randles–Ševčík equation, and the *b*-value of 1.0 corresponds to an ideally surface-controlled current that can originate from double-layer capacitance and/or fast surface redox processes [43, 44]. Note that the *b*-value analysis is a tool to estimate kinetic limitations within the probed range of sweep rates, but cannot determine the charge storage mechanism itself. Pristine HTO electrodes exhibit *b*-values of 0.52–0.67 (Figure 2D), consistent with predominantly diffusion-limited Na^+ storage. Note that here, only sweep rates ≤ 2 mV/s were analyzed due to rapid current degradation at higher rates. In contrast, expanded HTO-PA and HTO-OA maintain rectangular CV shapes up to at least 20 mV/s and quasi-rectangular CV shapes up to even 100 mV/s (Figure 2E,F). The CVs only show minor distortions at elevated rates, indicative of rapid kinetics, particularly for HTO-OA. Their *b*-values range from 0.81–0.96 (HTO-PA) and 0.89–0.98 (HTO-OA), revealing predominantly surface-controlled kinetics with minimal diffusion limitation across the probed rate range.

TABLE 1 | Interfacial resistances (R_{SEI}) and charge transfer resistances (R_{ct}) including fit errors extracted via equivalent circuit modelling of HTO, HTO-PA, and HTO-OA electrodes after the first sodiation (at 0.2 V vs. Na^+/Na) in either 1 M $NaPF_6$ in EC/PC or 2G electrolyte, carried out in three-electrode cells at 20°C.

Materials	R_{SEI} (Ω)		R_{ct} (Ω)	
	EC/PC	2G	EC/PC	2G
HTO	30.5 ± 0.25	3.1 ± 0.16	101.8 ± 1.34	6.6 ± 0.08
HTO-PA	88.0 ± 0.54	0.6 ± 0.09	451.0 ± 5.09	2.7 ± 0.21
HTO-OA	99.1 ± 0.56	n/a	193.8 ± 2.46	3.4 ± 0.16

A detailed kinetic analysis up to 100 mV/s using the *b*-value method is provided in Figure S6, demonstrating increasingly surface-limited kinetics at higher interlayer expansion.

Together, the evolution of CV/GCD profiles, the reduced impedance, and the high *b*-values collectively support a mechanism in which interlayer expansion enables solvent co-intercalation of Na^+-diglyme complexes. This process bypasses typically sluggish desolvation, and ion diffusion within the host electrode is supported by increased interlayer spacing, resulting in surface-limited kinetics. Importantly, this trend does not imply a precise geometric matching between solvent size and interlayer spacing, but it reflects progressively reduced confinement constraints within the larger galleries. The negligible interfacial impedance further indicates that dense passivation layers (that would act as barriers to solvent co-intercalation) are largely suppressed in diglyme (further analysis in later sections). In this context, the three-electrode EIS analysis provides the most direct evidence for the kinetic transition, because it resolves both the interfacial resistance and the charge transfer resistance of the HTO-based working electrode, which are the key quantities relevant to the observed shift toward capacitor-like behavior.

3.3 | Electrochemical Na^+ Storage in Conventional, Carbonate-Based Electrolyte

The analysis in the previous section demonstrates a transition toward sodium storage with capacitor-like electrochemical signatures as the HTO host lattice is progressively expanded. These fast kinetics were attributed to strongly suppressed interphase formation, enabled by the stability of Na^+-diglyme solvation structures that facilitate co-intercalation. To isolate the impact of the electrolyte solvation environment, the electrochemical process is now contrasted with that in a standard carbonate-based electrolyte, 1 M $NaPF_6$ in ethylene carbonate/propylene carbonate (EC/PC), which is known to form more resistive interphases on titanate-based electrodes at strongly reductive potentials [45]. It should be noted that the purpose of this comparison is not to directly extract nanoconfinement trends across different electrolyte systems, but to investigate a contrasting case that highlights how pronounced interphase formation impacts the efficiency and reversibility of solvent co-intercalation.

CVs of the HTO materials series exhibit pronounced redox peaks for pristine HTO at around 0.3–0.4 and 0.9–1.1 V versus Na^+/Na (Figure 3A). Expanded HTOs display broadened, somewhat rectangular CV signatures; however, in carbonates, these are less symmetric, exhibit resistive features, and show reduced current even at a slow sweep rate of 0.2 mV/s compared to diglyme electrolyte. This indicates significantly reduced reaction kinetics in carbonate electrolyte, particularly for the most expanded HTO-OA material.

GCD experiments at a rate of 50 mA/g reveal maximum anodic/desodiation capacities of 103, 119, and 105 mAh/g for HTO, HTO-PA, and HTO-OA electrodes, corresponding to 1.37 Na^+, 1.84 Na^+, and 2.12 Na^+ per tetratitanate unit. Although these capacities are comparable to those obtained in diglyme, the rate performance at elevated currents differs significantly. At higher GCD rates, the capacity for all electrodes fades rapidly. This effect is most pronounced for HTO-OA, whose rapid capacity loss contrasts sharply with its excellent rate response in diglyme and underscores the limitations imposed by carbonate electrolytes.

To elucidate the origins of the significantly worsened kinetics in carbonate electrolyte, EIS analysis was carried out after the first electrochemical reduction to 0.2 V versus Na^+/Na (Figure 3C). The Nyquist plots show pronounced semicircles in the mid-frequency region, indicative of substantial interfacial and charge transfer resistance. Whereas expanded HTO-PA and HTO-OA exhibited negligible R_{SEI} and R_{ct} in diglyme, the carbonate electrolyte produced large resistances, even exceeding those of pristine HTO (Table 1). Additional discussion of the impedance analysis of in carbonate electrolytes is also provided in Figure S5.

Moreover, the stability of the formed interphases is investigated by recording impedance spectra after subsequent cycles (Figure S7). For pristine HTO, highly reproducible Nyquist plots are recorded after up to 20 cycles, indicating the formation of a resistive yet stable SEI layer (Figure S7A). In contrast, HTO-PA and HTO-OA exhibit progressively increasing impedance in both mid- and low-frequency regions with cycling (Figure S7B,C), indicative of growing R_{SEI}, unstable interphase growthwith continued electrolyte decomposition. This suggests that expanded interlayers promote additional electrolyte reduction both at the particle surface and within the interlayer galleries, effectively extending the electrochemically reactive interface.

Collectively, the results show that carbonate electrolyte promotes substantial SEI formation. The presence of dense interphases prevents rapid solvent co-intercalation reactions and diminishes performance, particularly for highly expanded HTO electrodes. Furthermore, the instability of the electrolyte at reductive electrode potentials leads to continued side reactions and increasing impedance over cycling for expanded HTO. This behavior

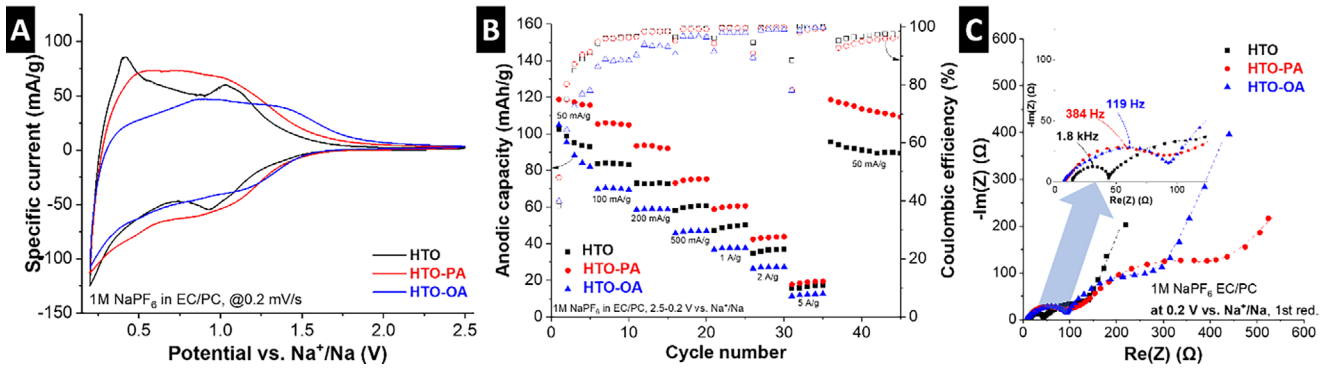

FIGURE 3 | Electrochemical characterization of HTO series in 1 M $NaPF_6$ in EC/PC electrolyte. (A) Cyclic voltammograms at 0.2 mV/s, (B) galvanostatic charge–discharge at rates from 50 mA/g to 5 A/g. (C) Nyquist plots recorded at stabilized electrode potentials of 0.2 V versus Na^+/Na, inset: zoomed-in view of mid-/high-frequency region.

contrasts sharply with the largely SEI-free and capacitor-like solvent co-intercalation regime in diglyme electrolyte, highlighting that both electrolyte solvation and interlayer structure jointly govern the charge storage mechanism in nanoconfined hosts.

3.4 | Mechanistic Investigation of Interphase Formation and Solvent Co-Intercalation

The electrochemical characterization revealed the strong influence of the host electrode's nanoconfinement properties and the electrolyte solvation environment on the resulting interphase formation and charge storage kinetics. We hypothesized that strongly suppressed interphase formation in diglyme electrolyte is a key enabler of the observed capacitor-like Na^+ intercalation kinetics. To verify this, ex situ transmission electron microscopy (TEM) investigations were carried out on pristine and expanded HTO electrodes after the first reduction to 0.2 V.

For these experiments, HTO-based materials were drop-cast directly onto TEM grids, which then served as working electrodes during sodiation in a Swagelok-type three-electrode cell. After electrochemical reduction via linear sweep voltammetry at 0.5 mV/s and holding at 0.2 V for 2 h to ensure complete sodiation/interphase formation, the cells were reopened in an Ar-filled glovebox, the grids removed and rinsed with the corresponding electrolyte solvent (PC or diglyme) for residual salt removal, and placed into an inert-transfer-holder, allowing transfer into the microscope without air exposure [46].

A comparison between pristine HTO sodiated at 0.2 V in carbonate-based electrolyte (Figure 4A) and diglyme-based electrolyte (Figure 4B) reveals pronounced differences in surface structure and chemistry. High-resolution TEM (HR-TEM) imaging shows the formation of a several nanometer-thick amorphous surface layer across the rod-shaped HTO particles, indicative of significant SEI formation in carbonate electrolyte. This is corroborated by EDX in scanning TEM (STEM) mode. The presence of substantial fluorine (~6–7 at.%) and phosphorus (~1–1.5 at.%) at the particle surface is consistent with salt-derived inorganic SEI components formed from $NaPF_6$ decomposition, including NaF and phosphate/fluorophosphate species [47, 48].

In contrast, using diglyme electrolyte, no visible amorphous surface layers are detected via HRTEM, and the elemental mapping reveals significantly reduced fluorine (<2 at.%) and phosphorus (<1 at.%) contents, indicating strongly reduced electrolyte decomposition products. These localized results are consistent with the impedance spectra recorded at analogous states of charge, which globally showed interfacial resistances R_{SEI} that are orders of magnitude lower in diglyme relative to carbonate electrolyte (Table 1). This interpretation is also consistent with recent photoelectron spectroscopy studies on titanate-based sodium-ion anodes, which showed that diglyme-based electrolytes form thinner, more stable, and less resistive interphases than carbonate-based electrolytes [45].

In highly expanded HTO-OA, the TEM observations follow the same electrolyte-dependent trend as observed for pristine HTO. HTO-OA sodiated in carbonate electrolyte shows large amorphous surface regions (Figure 4C), whereas HTO-OA cycled in diglyme shows sharply defined particle surfaces (Figure 4D). It should be noted that partial decomposition of OA pillars under the electron beam can complicate an unambiguous interpretation of HRTEM images. The elemental composition from STEM-EDX also confirms reduced formation of typical inorganic SEI components in diglyme electrolyte, with significantly lower fluorine- and phosphorus-contents compared to carbonate electrolyte.

Finally, the charge storage mechanism of HTO and HTO-OA in the two electrolytes is examined, with particular focus on the participation of the solvent co-intercalation mechanism. Operando electrochemical dilatometry (ECD) is employed to probe the global electrode thickness changes during cycling (Figure 5), providing indirect insight into particle-level volume changes associated with Na^+ insertion [49, 50]. A direct quantification of the amount of co-intercalated solvent is not straightforward in the present HTO system. Upon sodiation, the materials rapidly lose long-range crystalline order, which limits a reliable diffraction-based analysis of solvent uptake. Trial electrochemical quartz crystal microbalance (EQCM) measurements in the relevant low-potential regime were dominated by parasitic interfacial processes and did not allow a robust gravimetric interpretation. We therefore use ECD here as a complementary probe that does not rely on preserved crystallinity and can still sensitively capture

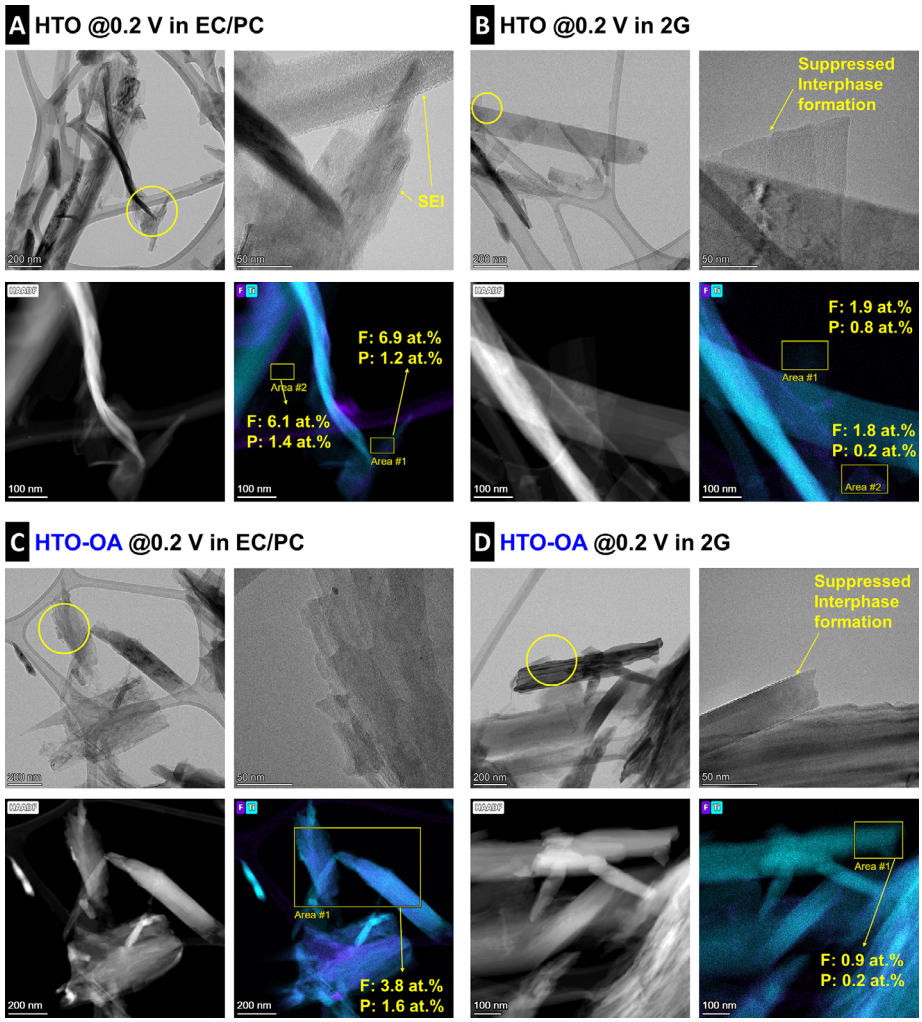

FIGURE 4 | Ex situ TEM investigations of HTO and HTO-OA electrode materials after first sodiation at an electrode potential of 0.2 V versus Na^+/Na, held for 2 h. BF-TEM (region highlighted in yellow circle is shown as a magnified HRTEM image), HAADF-STEM, and STEM-EDX mapping of Ti (teal) and F (purple) signals of (A) HTO in carbonate, (B) HTO in diglyme, (C) HTO-OA in carbonate, and (D) HTO-OA in diglyme electrolyte.

the large electrode expansion expected for solvent participation in the intercalation process.

We first compare the dilatometric response of pristine HTO in EC/PC (Figure 5A) and diglyme electrolyte (Figure 5B). In carbonate electrolyte, only minimal electrode expansion is detected, with an initial increase of ~3.7% and subsequent reversible changes below 0.5% during cycling. In contrast, HTO in diglyme exhibits a pronounced expansion of 13.4% during the initial sodiation, followed by partial contraction to 8.9% upon desodiation and reversible height changes of ±3%–5% in subsequent cycles. The markedly larger volume response in diglyme is consistent with a transition from desolvated Na^+ intercalation in EC/PC to solvent co-intercalation, where insertion of solvated Na^+-diglyme complexes drives substantial lattice expansion [12, 51]. The irreversible component of the first cycle expansion suggests that a fraction of species remains trapped within the interlayer galleries after desodiation.

For HTO-OA in EC/PC (Figure 5C), an expansion of ~6% is observed during the initial sodiation, followed by a continued increase to ~8.9% during desodiation, indicative of electrolyte uptake and irreversible interphase formation rather than reversible solvent co-intercalation. In subsequent cycles, however, volume changes are strongly suppressed (<1%). We attribute this behavior to the formation of severely blocking interphases, consistent with the large and growing interfacial impedances observed by EIS, which prevent further reversible solvent insertion.

This behavior contrasts sharply with HTO-OA in diglyme electrolyte (Figure 5D). Here, an initial expansion of 6.6% is followed by contraction to 4% upon desodiation, and reversible thickness changes of approximately ±3%–4% are maintained over subsequent cycles. The partially irreversible expansion remaining after the first cycle is attributed mainly to partial trapping or incomplete removal of co-intercalated solvent-containing species within the highly expanded interlayer galleries after the initial sodiation/desodiation process. This response is otherwise characteristic of highly reversible solvent co-intercalation in expanded interlayer galleries [12]. While ECD does not provide a direct quantitative solvent-to-ion ratio, the strong contrast between carbonate and diglyme electrolytes provides robust qualitative evidence for substantial solvent participation in the latter case.

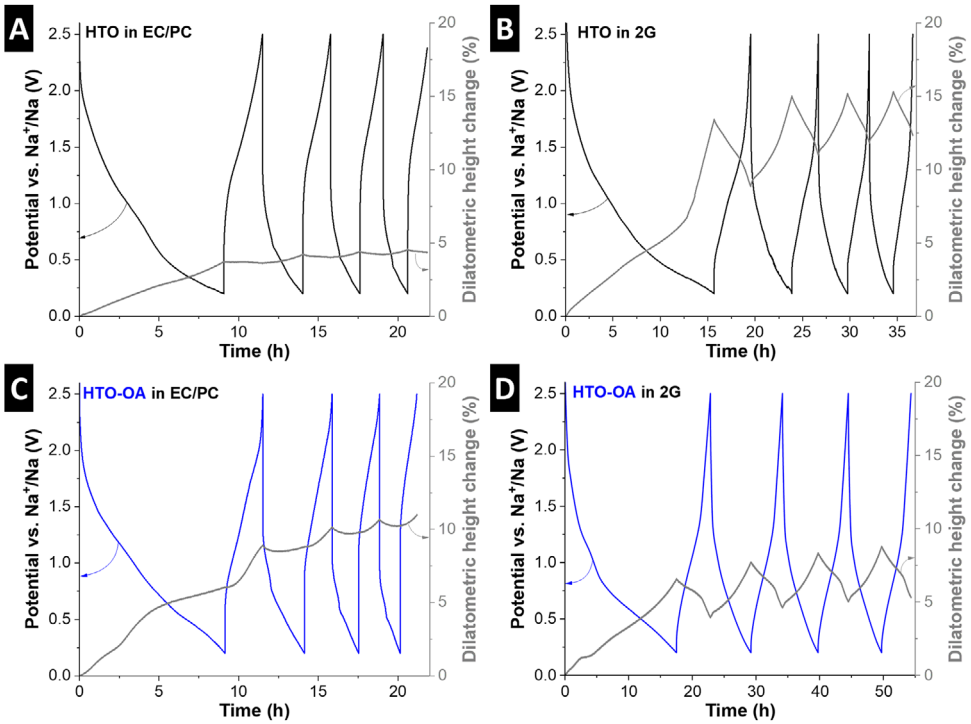

FIGURE 5 | Operando electrode height measurement via electrochemical dilatometry over four cycles in galvanostatic mode at 20 mA/g. (A) HTO electrode in EC/PC, (B) HTO electrode in diglyme, (C) HTO-OA electrode in EC/PC, and (D) HTO-OA electrode in diglyme electrolyte. Measurements were conducted at a constant temperature of 22°C.

Taken together, the combined EIS, TEM/EDX, and operando dilatometry results show that the capacitor-like Na^+ storage behavior in diglyme is explained by suppressed interphase formation and solvent co-intercalation in the expanded HTO galleries. The key evidence for the kinetic transition is provided by the three-electrode EIS analysis, while TEM/EDX and operando dilatometry provide complementary support for suppressed SEI formation and solvent co-intercalation, respectively.

4 | Conclusions

In this work, we demonstrate how interlayer nanoconfinement and electrolyte solvation jointly govern the Na^+ storage mechanism using layered hydrogen titanates as a model system. By systematically expanding the interlayer galleries and comparing carbonate and diglyme electrolytes, we establish a clear mechanistic transition from conventional, diffusion-limited intercalation in carbonate electrolyte to a fast, capacitor-like solvent co-intercalation regime in diglyme. Expanded HTO structures exhibit rectangular CV signatures, ultralow charge transfer resistance, and high-rate capability, all of which arise from the co-intercalation of Na^+-diglyme complexes and strongly suppressed formation of dense, blocking interphases. In contrast, carbonate electrolytes promote substantial and unstable interphase formation, particularly in expanded HTOs, leading to rapid degradation and low-rate performance. These effects become increasingly detrimental at larger interlayer spacings.

Ex situ TEM/EDX and operando dilatometry confirm the stark divergence in interphase chemistry and volumetric response between the two electrolyte systems, providing direct evidence of suppressed electrolyte decomposition and reversible, co-intercalation-induced swelling when using diglyme. Together, these findings offer experimental validation of the predicted confinement-controlled continuum between Faradaic and capacitor-like charge storage and highlight the need for both electrolyte solvation and nanoconfinement design as a powerful strategy for enabling high-rate Na^+ storage.

The insights gained in this work suggest that coupling structural confinement with tailored electrolyte solvation may unlock new classes of interphase-suppressed, pseudocapacitive intercalation electrodes, offering a promising design paradigm for future high-power sodium-ion batteries and/or hybrid supercapacitor devices.

Author Contributions

M. E., S., T. P., J. K., and M. T. performed materials synthesis, SEM, XRD, and TGA analysis. M. E., S., and M. T. conducted standard electrochemical measurements (CV, GCD). Y. T. M. conducted the impedance study. Y. T. M. and J. C. conducted ECD measurements. Y. T. M. prepared the samples for, and R. L. conducted the microscopy investigation for the ex-situ TEM part. X. L. and D.-E. J. conducted the theoretical study. M. T., W.-Y. T., D.-E. J., and S. F. supervised the work. S. F. wrote the manuscript, with help from all co-authors.

Acknowledgements

Y.T.M. and S.F. acknowledge funding from the German Research Foundation (DFG) in the project "NanoconEC" (project number 513327636). Y.T.M., M.E., M.T., and S.F. acknowledge funding from the German Federal Ministry of Research, Technology and Space (BMFTR) in the

NanoMatFutur program (Grant Number 03XP0423) and financial support from the Helmholtz Association. M.E. acknowledges financial support from the Karlsruhe House of Young Scientists (KHYS) Research Travel Grant. S.F. thanks the Daimler and Benz Foundation for financial support in the Scholarship program. W.-Y.T. was supported by the French National Agency for Research (ANR) through Chaire de Professeur Junior funding and RS2E network (STORE-EX Labex Project ANR-10-LABX-76-01). D.-E.J. and X.L. were supported by the National Science Foundation (Award number: DMR-2221646).

Open access funding enabled and organized by Projekt DEAL.

Conflicts of Interest

The authors declare no conflicts of interest.

Data Availability Statement

Experimental data used in this work are made available on the Zenodo repository (https://zenodo.org) under https://doi.org/10.5281/zenodo.20728620.

References

1. R. Usiskin, Y. Lu, J. Popovic, et al., "Fundamentals, Status and Promise of Sodium-Based Batteries," *Nature Reviews Materials* 6 (2021): 1020–1035, https://doi.org/10.1038/s41578-021-00324-w.

2. F. Xie, Z. Xu, Z. Guo, and M. M. Titirici, "Hard Carbons for Sodium-Ion Batteries and Beyond," *Progress in Energy* 2 (2020): 042002, https://doi.org/10.1088/2516-1083/aba5f5.

3. B. Babu, P. Simon, and A. Balducci, "Fast Charging Materials for High Power Applications," *Advanced Energy Materials* 10 (2020): 2001128, https://doi.org/10.1002/aenm.202001128.

4. M. M. Doeff, J. Cabana, and M. Shirpour, "Titanate Anodes for Sodium Ion Batteries," *Journal of Inorganic and Organometallic Polymers and Materials* 24 (2014): 5–14, https://doi.org/10.1007/s10904-013-9977-8.

5. W. Yin, J. Ahn, G. Barim, J. Alvarado, and M. M. Doeff, "Tailoring Stepped Layered Titanates for Sodium-Ion Battery Applications," *Accounts of Materials Research* 5 (2024): 933–943, https://doi.org/10.1021/accountsmr.4c00080.

6. X. Zheng, P. Li, H. Zhu, et al., "Understanding the Structural and Chemical Evolution of Layered Potassium Titanates for Sodium Ion Batteries," *Energy Storage Materials* 25 (2020): 502–509, https://doi.org/10.1016/j.ensm.2019.09.032.

7. P. Senguttuvan, G. Rousse, V. Seznec, J. M. Tarascon, and M. R. Palacin, "$Na_2Ti_3O_7$: Lowest Voltage Ever Reported Oxide Insertion Electrode for Sodium Ion Batteries," *Chemistry of Materials* 42 (2011): 4109–4111, https://doi.org/10.1021/cm202076g.

8. H. Izawa, S. Kikkawa, and M. Koizumi, "Ion Exchange and Dehydration of Layered [Sodium and Potassium] Titanates, $Na_2Ti_3O_7$ and $K_2Ti_4O_9$," *The Journal of Physical Chemistry* 86 (1982): 5023–5026, https://doi.org/10.1021/j100222a036.

9. A. Eguía-Barrio, E. Castillo-Martínez, M. Zarrabeitia, M. A. Muñoz-Márquez, M. Casas-Cabanas, and T. Rojo, "Structure of $H_2Ti_3O_7$ and Its Evolution During Sodium Insertion as Anode for Na Ion Batteries," *Physical Chemistry Chemical Physics* 17 (2015): 6988–6994, https://doi.org/10.1039/c4cp03345k.

10. S. Fleischmann, Y. Sun, N. C. Osti, et al., "Interlayer Separation in Hydrogen Titanates Enables Electrochemical Proton Intercalation," *Journal of Materials Chemistry A* 8 (2020): 412–421, https://doi.org/10.1039/c9ta11098d.

11. S. Saeed, S. Fleischmann, T. Kobayashi, et al., "Oxide Acidity Modulates Structural Transformations in Hydrogen Titanates during Electrochemical Li-Ion Insertion," *Journal of the American Chemical Society* 146 (2024): 28795–28808, https://doi.org/10.1021/jacs.4c08063.

12. M. Elmanzalawy, H. Song, M. Tobis, et al., "Nanoconfinement-Induced Electrochemical Ion-Solvent Cointercalation in Pillared Titanate Host Materials," *Angewandte Chemie International Edition* 64 (2025): 202423593, https://doi.org/10.1002/anie.202423593.

13. M. Piao, S. M. Oh, J. Lim, et al., "Critical Role of the Chemical Environment of Interlayer Na Sites: an Effective Way to Improve the Na Ion Electrode Activity of Layered Titanate," *ACS Applied Materials & Interfaces* 10 (2018): 33112–33123, https://doi.org/10.1021/acsami.8b07031.

14. H. Guo, M. Elmanzalawy, P. Sivakumar, and S. Fleischmann, "Unifying Electrolyte Formulation and Electrode Nanoconfinement Design to Enable New Ion–Solvent Cointercalation Chemistries," *Energy & Environmental Science* 17 (2024): 2100–2116, https://doi.org/10.1039/d3ee04350a.

15. G. A. Ferrero, G. Åvall, K. Janßen, et al., "Solvent Co-Intercalation Reactions for Batteries and beyond," *Chemical Reviews* 125 (2025): 3401–3439, https://doi.org/10.1021/acs.chemrev.4c00805.

16. B. Jache and P. Adelhelm, "Use of Graphite as a Highly Reversible Electrode with Superior Cycle Life for Sodium-Ion Batteries by Making Use of Co-Intercalation Phenomena," *Angewandte Chemie International Edition* 53 (2014): 10169–10173, https://doi.org/10.1002/anie.201403734.

17. B. Jache, J. O. Binder, T. Abe, and P. Adelhelm, "A Comparative Study on the Impact of Different Glymes and Their Derivatives as Electrolyte Solvents for Graphite Co-Intercalation Electrodes in Lithium-Ion and Sodium-Ion Batteries," *Physical Chemistry Chemical Physics* 18 (2016): 14299–14316, https://doi.org/10.1039/c6cp00651e.

18. M. Goktas, C. Bolli, E. J. Berg, et al., "Graphite as Cointercalation Electrode for Sodium-Ion Batteries: Electrode Dynamics and the Missing Solid Electrolyte Interphase (SEI)," *Advanced Energy Materials* 8 (2018): 1702724, https://doi.org/10.1002/aenm.201702724.

19. X. Huang, Y. F. Cheng, H. Liu, et al., "Interlayer Confined Capacitive Response via Solvated Cointercalation in Graphite Layers," *ACS Nano* 19 (2025): 7168–7177, https://doi.org/10.1021/acsnano.4c16593.

20. X. Huang, Z. Yan, X. Chang, D. Tang, and Q. Wei, "Size Effect of Graphite Anode with Boosted Capacitive Solvated-Na^+ Co-Intercalation for High-Power Sodium-Ion Capacitors," *Chinese Chemical Letters* 37 (2026): 110953, https://doi.org/10.1016/j.cclet.2025.110953.

21. S. Fleischmann, Y. Zhang, X. Wang, et al., "Continuous Transition from Double-Layer to Faradaic Charge Storage in Confined Electrolytes," *Nature Energy* 7 (2022): 222–228, https://doi.org/10.1038/s41560-022-00993-z.

22. D. Weingarth, M. Zeiger, N. Jäckel, M. Aslan, G. Feng, and V. Presser, "Graphitization as a Universal Tool to Tailor the Potential-Dependent Capacitance of Carbon Supercapacitors," *Advanced Energy Materials* 4 (2014): 1400316, https://doi.org/10.1002/aenm.201400316.

23. G. Kresse and J. Hafner, "Ab Initio Molecular Dynamics for Liquid Metals," *Physical Review B* 47 (1993): 558–561, https://doi.org/10.1103/PhysRevB.47.558.

24. G. Kresse and J. Furthmüller, "Efficient Iterative Schemes for Ab Initio Total-Energy Calculations Using a Plane-Wave Basis Set," *Physical Review B* 54 (1996): 11169–11186, https://doi.org/10.1103/PhysRevB.54.11169.

25. G. Kresse and J. Furthmüller, "Efficiency of Ab-Initio Total Energy Calculations for Metals and Semiconductors Using a Plane-Wave Basis Set," *Computational Materials Science* 6 (1996): 15–50, https://doi.org/10.1016/0927-0256(96)00008-0.

26. G. Kresse and D. Joubert, "From Ultrasoft Pseudopotentials to the Projector Augmented-Wave Method," *Physical Review B* 59 (1999): 1758–1775, https://doi.org/10.1103/PhysRevB.59.1758.

27. J. P. Perdew, K. Burke, and M. Ernzerhof, "Generalized Gradient Approximation Made Simple," *Physical Review Letters* 77 (1996): 3865–3868, https://doi.org/10.1103/PhysRevLett.77.3865.

28. V. Wang, N. Xu, J.-C. Liu, G. Tang, and W.-T. V. Geng, "VASPKIT: A User-friendly Interface Facilitating High-throughput Computing and

Analysis Using VASP Code," *Computer Physics Communications* 267 (2021): 108033, https://doi.org/10.1016/j.cpc.2021.108033.

29. S. Grimme, J. Antony, S. Ehrlich, and H. Krieg, "A Consistent and Accurate Ab Initio Parametrization of Density Functional Dispersion Correction (DFT-D) for the 94 Elements H-Pu," *The Journal of Chemical Physics* 132 (2010): 154104, https://doi.org/10.1063/1.3382344.

30. K. Momma and F. Izumi, "VESTA 3 for Three-Dimensional Visualization of Crystal, Volumetric and Morphology Data," *Journal of Applied Crystallography* 44 (2011): 1272–1276, https://doi.org/10.1107/S0021889811038970.

31. H. Izawa, S. Kikkawa, and M. Koizumi, "Formation and Properties of N-Alkylammonium Complexes with Layered Tri- and Tetra-Titanates," *Polyhedron* 2 (1983): 741–744, https://doi.org/10.1016/S0277-5387(00)87201-0.

32. T. Gao, H. Fjellvåg, and P. Norby, "Crystal Structures of Titanate Nanotubes: A Raman Scattering Study," *Inorganic Chemistry* 48 (2009): 1423–1432, https://doi.org/10.1021/ic801508k.

33. H. Guo, M. Sotoudeh, S. Rezeki, et al., "Regulating Solvent Co-Intercalation in Bi-Layered Vanadium Oxides for Zinc Batteries by Nanoconfinement Chemistry," *Angewandte Chemie* 65 (2025): 20990, https://doi.org/10.1002/anie.202520990.

34. M. M. Leite, V. L. Martins, F. M. Vichi, and R. M. Torresi, "Electrochemistry of Sodium Titanate Nanotubes as a Negative Electrode for Sodium-Ion Batteries," *Electrochimica Acta* 331 (2020): 135422, https://doi.org/10.1016/j.electacta.2019.135422.

35. H. Banda, S. Périé, B. Daffos, et al., "Sparsely Pillared Graphene Materials for High-Performance Supercapacitors: Improving Ion Transport and Storage Capacity," *ACS Nano* 13 (2019): 1443–1453, https://doi.org/10.1021/acsnano.8b07102.

36. J. Choi, K. Nam, Y. T. Malik, et al., "Interlayer Spacing Control of MoS_2 with Covalent Thiol Functionalization: Understanding Structure and Electrochemistry from Experiments and Simulation," *ACS Nano* 19 (2025): 35425–35437, https://doi.org/10.1021/acsnano.5c07717.

37. S. Fleischmann, H. Shao, P.-L. L. Taberna, P. Rozier, and P. Simon, "Electrochemically Induced Deformation Determines the Rate of Lithium Intercalation in Bulk TiS_2," *ACS Energy Letters* 6 (2021): 4173–4178, https://doi.org/10.1021/acsenergylett.1c01934.

38. P.-L. L. Taberna, P. Simon, and J. F. Fauvarque, "Electrochemical Characteristics and Impedance Spectroscopy Studies of Carbon-Carbon Supercapacitors," *Journal of the Electrochemical Society* 150 (2003): A292, https://doi.org/10.1149/1.1543948.

39. P. M. Chekushkin, I. S. Merenkov, V. S. Smirnov, S. A. Kislenko, and V. A. Nikitina, "The Physical Origin of the Activation Barrier in Li-Ion Intercalation Processes: The Overestimated Role of Desolvation," *Electrochimica Acta* 372 (2021): 137843, https://doi.org/10.1016/j.electacta.2021.137843.

40. W. Choi, H.-C. Shin, J. M. Kim, J.-Y. Choi, and W.-S. Yoon, "Modeling and Applications of Electrochemical Impedance Spectroscopy (EIS) for Lithium-Ion Batteries," *Journal of Electrochemical Science and Technology* 11 (2020): 1–13, https://doi.org/10.33961/jecst.2019.00528.

41. J. Wang, J. Polleux, J. Lim, and B. Dunn, "Pseudocapacitive Contributions to Electrochemical Energy Storage in TiO_2 (Anatase) Nanoparticles," *The Journal of Physical Chemistry C* 111 (2007): 14925–14931, https://doi.org/10.1021/jp074464w.

42. H. Lindström, S. Södergren, A. Solbrand, et al., "Li+ Ion Insertion in TiO_2 (Anatase). 2. Voltammetry on Nanoporous Films," *The Journal of Physical Chemistry B* 101 (1997): 7717–7722, https://doi.org/10.1021/jp970490q.

43. A. J. Bard and L. R. Faulkner, *Electrochemical Methods: Fundamentals and Applications* (John Wiley & Sons, 2000).

44. S. Fleischmann, J. B. Mitchell, R. Wang, et al., "Pseudocapacitance: From Fundamental Understanding to High Power Energy Storage Materials," *Chemical Reviews* 120 (2020): 6738–6782, https://doi.org/10.1021/acs.chemrev.0c00170.

45. L. Zhao, S. I. R. Costa, Y. Chen, et al., "A Comparative Study of Solid Electrolyte Interphase Evolution in Ether and Ester-Based Electrolytes for Na-Ion Batteries," *PRX Energy* 4 (2025): 033002, https://doi.org/10.1103/jfvb-wp5w.

46. Y. Shin, D. Stepien, M. Hepp, B. Butz, D. Bresser, and S. Fleischmann, "Cryogenic Electron Microscopy Workflows for the Characterization of Electrochemical Interfaces and Interphases in Batteries," *Journal of Power Sources* 556 (2023): 232515, https://doi.org/10.1016/j.jpowsour.2022.232515.

47. B. Han, Y. Zou, Z. Zhang, et al., "Probing the Na Metal Solid Electrolyte Interphase via Cryo-Transmission Electron Microscopy," *Nature communications* 12 (2021): 3066, https://doi.org/10.1038/s41467-021-23368-6.

48. F. Cheng, J. Hu, W. Zhang, et al., "Reviving Ether-Based Electrolytes for Sodium-Ion Batteries," *Energy & Environmental Science* 18 (2025): 6874–6898, https://doi.org/10.1039/d5ee00725a.

49. I. Escher, M. Hahn, G. A. Ferrero, and P. Adelhelm, "A Practical Guide for Using Electrochemical Dilatometry as Operando Tool in Battery and Supercapacitor Research," *Energy Technology* 10 (2022): 2101120, https://doi.org/10.1002/ente.202101120.

50. Y. T. Malik, J. Yang, J. Choi, et al., "Correlating (Chemo-)Mechanical Coupling in TiS_2 during Li^+ Intercalation across Liquid and Solid Electrolytes via Operando Analysis," *ACS Energy Letters* (2026): 1651–1658, https://doi.org/10.1021/acsenergylett.5c02943.

51. I. Escher, Y. Kravets, G. A. Ferrero, M. Goktas, and P. Adelhelm, "Strategies for Alleviating Electrode Expansion of Graphite Electrodes in Sodium-Ion Batteries Followed by in Situ Electrochemical Dilatometry," *Energy Technology* 9 (2021): 2000880, https://doi.org/10.1002/ente.202000880.

Supporting Information

Additional supporting information can be found online in the Supporting Information section.

Supporting File: aenm71245-sup-0001-SuppMat.pdf.